Chemical Science

ROYAL SOCIETY OF CHEMISTRY

EDGE ARTICLE

View Article Online
View Journal

Cite this: DOI: 10.1039/d6sc02703b

All publication charges for this article have been paid for by the Royal Society of Chemistry

Constructing an interconnected gel with ionic fluid channels for AC line-filtering

Jie zhang,[a] Zhuanpei Wang*[b] and Xiaowei Yang *[a]

Electric double-layer capacitors operating at 120 Hz are promising alternatives to bulky aluminum electrolytic capacitors for AC line-filtering. However, a pivotal challenge in developing high-performance filtering electrodes is achieving the rapid ion response of pathways without compromising high capacity. Here, we construct a 3D interconnected gel framework consisting of reduced graphene oxide (rGO) and carboxylated multi-walled carbon nanotubes (MWCNTs), featuring ionic fluid channels. The mixed MWCNTs effectively inhibit the re-stacking of rGO, forming an interconnected open network that ensures high-density electron transport and ultra-fast ionic accessibility. Systematic investigations reveal that the electrochemical performance is governed by a synergistic balance among conductive continuity, interfacial wettability, and open fluid ion-transport channels. The optimized electrode achieves an ultralow series resistance of 43.5 mΩ cm^2 and a high areal capacitance of 3.56 mF cm^{-2} at 120 Hz ($\varphi = -81.1°$). This study is the first to apply fluid gel channels to filtering capacitors, providing a reliable theoretical basis for advanced carbon-based electrochemical capacitors in the next generation of power electronic systems.

Received 1st April 2026
Accepted 20th April 2026

DOI: 10.1039/d6sc02703b

rsc.li/chemical-science

Introduction

Electric double-layer capacitors (EDLCs) operating at 120 Hz are emerging as critical alternatives to bulky aluminum electrolytic capacitors (AECs) for AC line-filtering in miniaturized electronics.[1,2] While AECs offer rapid response times, their extremely low capacitance density hinders the development of portable, high-density power systems. EDLCs provide a leap in energy density, yet traditional carbon electrodes are plagued by complex microporous structures (<2 nm) that restrict ion mobility, limiting their effective operation to frequencies below 1 Hz.[3–5] A seminal breakthrough by Miller *et al.* utilized vertically oriented graphene to demonstrate that wide-open vertical pathways could significantly enhance high-frequency ion diffusion.[1] However, these vertical architectures often suffer from a limited ion-storage surface area, resulting in an areal capacitance (C_A) of only 87.5 μF cm^{-2}. Subsequent efforts to improve C_A by increasing the height or density of vertical arrays have struggled to maintain a high volumetric capacitance (C_v), which remains stagnated between 1.1 and 1.5 F cm^{-3} due to the excessive void space required for high-frequency access.[6–9]

Loose ion-diffusion paths in the vertical structure are essential for frequency response, but high-density planar networks are required for high specific capacitance. While planar carbon networks (such as dense CNTs, PEDOT-derived carbon materials or graphene films) offer superior volumetric capacitance, they inevitably suffer from the restacking of nanosheets *via* strong π–π interactions.[10–14] These restacked compact lamellar structures severely impede ion penetration between layers, leading to high series resistance (R_s > 70 mΩ cm^2).[15] Although recent progress in mesoporous carbon has attempted to bridge this gap, most studies remain trapped in the trade-off between response capability and storage density.[16,17] Consequently, the central challenge in 120 Hz filtering lies in transcending this limitation by designing an electrode that maintains the high density of planar networks while incorporating open channels to eliminate mass transfer resistance. The research on hybridization of two-dimensional graphene with one-dimensional carbon nanotubes has been extensively explored in other fields. Researchers have used strategies such as electrostatic self-assembly, vacuum-assisted layer-by-layer filtration, and chemical vapor deposition to construct them into multi-scale composite materials.[18–22] However, most of these traditional methods can only yield simple physical mixtures or loosely supported structures. In such structures, the graphene sheets and carbon nanotubes either randomly aggregate or are unevenly distributed. Such non-integrated interfaces often suffer from high contact resistance and a lack of robust mechanical connectivity, which ultimately limits efficient charge transfer and rapid ion flux during high-frequency charging. Furthermore, simple filtration-based composites still cannot fully prevent the collapse of the mesoporous framework during the drying or electrode-pressing process.

[a]*School of Chemistry and Chemical Engineering, Shanghai Jiao Tong University, Shanghai 200240, P. R. China. E-mail: yangxw@sjtu.edu.cn*

[b]*School of Energy Science and Technology, Longzihu New Energy Laboratory, Zhengzhou Institute of Emerging Industrial Technology, Henan University, Zhengzhou, 450046, P. R. China. E-mail: zhuanpeiwang@henu.edu.cn*

In this work, we propose constructing a 3D interconnected gel framework *via* a controlled hydrothermal-filtration method, as described in our previous work.[23–25] Herein, a series of composite gel membranes composed of planar reduced graphene oxide (rGO) and supporting carboxylated multi-walled carbon nanotubes (MWCNTs) were fabricated to avoid the limitations of purely dense stacking or vertical alignment through the anchoring effect of the amino nitrogen on rGO and the continuous fluid channels within the framework. This specific integration allows the planar network to remain mechanically robust and dense enough for high capacity, while simultaneously creating a 3D interconnected open fluid network with enhanced interfacial wettability and ion-accessible channels. Our study reveals that the composite gel electrode with highly interconnected fluid channels successfully improves the long-standing trade-off between frequency response and capacity. As a result, the optimized G2C1 based EDLC achieved an ultralow R_s of 43.5 mΩ cm^2 and a high C_A of 3.56 mF cm^{-2} at 120 Hz, providing a robust design principle for next-generation, high-performance filtering capacitors.

Results and discussion

To address the challenges of high-frequency response, achieving a fast ion transport microenvironment within graphene-based electrode materials is of paramount importance. The high-density reduced graphene oxide membrane (rGM) typically used for capacitive storage often suffers from severe interlayer restacking; its internal channels undergo extreme contraction during the drying process, resulting in a high density of micropores and dead pores. These structural defects significantly impede the rapid migration of hydrated ions, leading to high total resistance (Fig. 1a, comprising both series resistance R_s and diffusion resistance R_d), which prevents the material from satisfying the stringent requirements for phase angle and capacitance in 120 Hz AC line-filtering. For high-frequency application-oriented EDLCs, the intersection point of the curve with the real axis in the high-frequency region represents R_s, including external circuit contact resistance, electrode resistance, electrolyte resistance, *etc*. In the medium-frequency region, R_d is estimated from the linear extrapolation of the almost vertical portion of the Nyquist plot to the real axis at low frequency, which reflects the diffusion process of ions in the electrode channels. While in the low-frequency region, it approaches a vertical line perpendicular to the real axis, representing the ideal capacitive behavior. The steeper the slope of the straight line, the better the capacitive characteristics (Fig. S1).

In contrast, our previous research demonstrated that the initial rGO gel (rGG^0), which retains a remarkably high-water content (94 wt%), maintains an open and continuous fluid network. Unlike the frozen structure of rGM, the rGG^0 framework provides abundant aqueous mesoporous channels that effectively resolve the interlayer confinement effect. Consequently, even though the electronic conductivity of rGG^0 decreases by two orders of magnitude (303 S cm^{-1} → 2.26 S cm^{-1}), the gel membrane electrode still exhibits excellent electron transfer performance, resulting from a low electrode resistance (0.398 mΩ cm^2) that accounted for less than 1% of R_s. Its fluid-filled internal architecture drastically enhances ionic mobility and significantly improves ionic conductivity. This leads to a concurrent reduction in both R_s and R_d, thereby enabling the desired high-frequency response.

As illustrated in Fig. 1b, to further minimize the ion migration distance, the rGG membrane was prepared through sulfuric acid exchange and subsequent evaporation of volatile components (detailed procedures are provided in Fig. S2). While the electrode thickness was reduced by half (Fig. S3), the non-volatile sulfuric acid effectively maintained the mesoporous regions within the electrode material, ensuring that

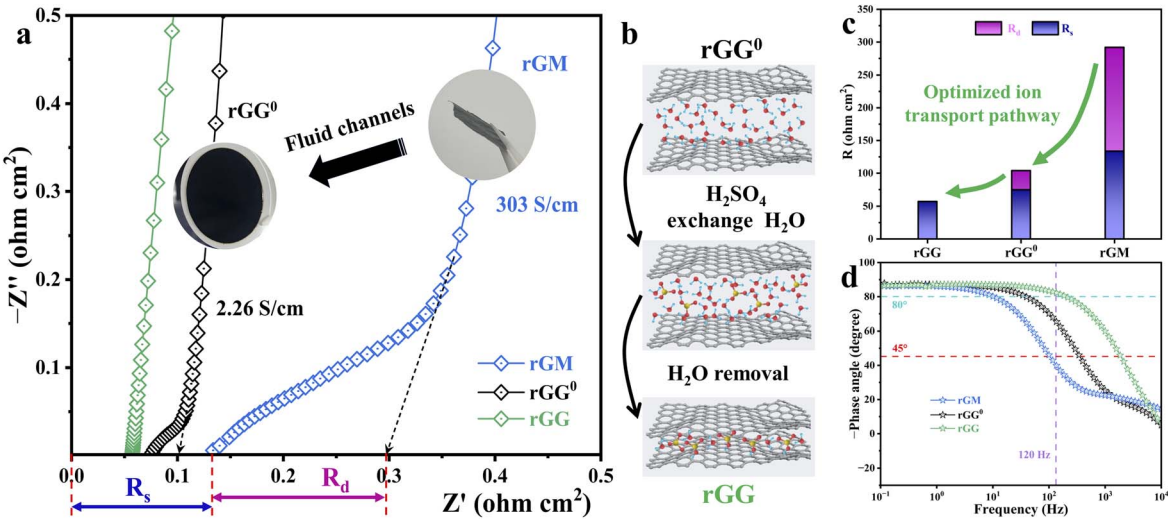

Fig. 1 Electrochemical characterization and structural evolution of rGM, rGG^0, and rGG. (a) Nyquist plots of rGM, rGG^0, and rGG. (b) Schematic illustration of the structural evolution from rGG^0 to rGG. (c) Comparison of resistance components (R_s and R_d) and (d) Bode plots for the three electrodes.

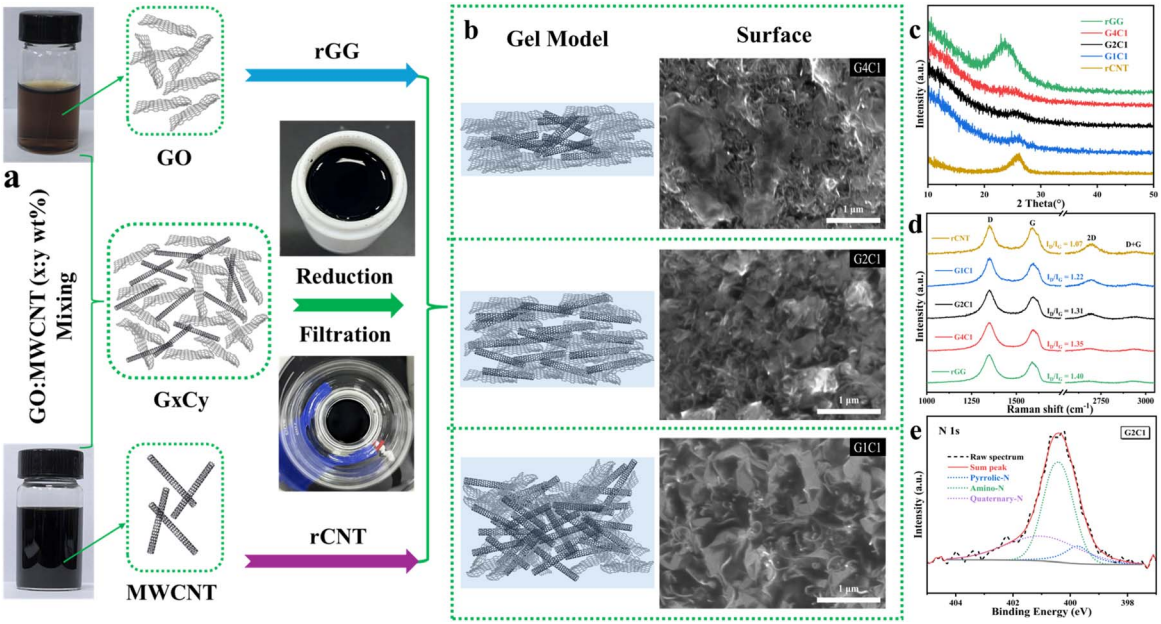

Fig. 2 Preparation and structural characterization of GxCy hybrid gels. (a) Schematic illustration of the hydrothermal self-assembly process. (b) Structural models and SEM images of G4C1, G2C1, and G1C1 hybrid gels. (c) XRD patterns and (d) Raman spectra of rGG, G4C1, G2C1, G1C1, and rCNT samples. (e) XPS N 1s spectrum of the G2C1 sample.

robust fluid pathways remained after subsequent electrolyte immersion. This wet-gel preservation strategy effectively maintained the intrinsic hydrated ionic diffusion pathways, laying the groundwork for ultrafast electrochemical kinetics. Finally, the symmetric gel based electric double layer capacitor (Gel-EDLC) was assembled by transfer-printing two processed gel electrodes onto Pt current collectors, integrated with a separator and the corresponding electrolyte. As a result, the total resistance of the assembled EDLC further decreased, and the diffusion resistance disappeared (Fig. 1c). The device exhibits exceptional ionic response performance, achieving an impedance phase angle of −82.9° at 120 Hz, as shown in the Bode diagram of Fig. 1d.

Although the rGG membrane significantly reduces ion transport resistance by maintaining a richly fluid network, the unsupported pure graphene sheets still exhibit a tendency toward local restacking at high frequencies. This structural limitation restricts the further exposure of the effective electroactive surface area, resulting in an areal capacitance of only 1.71 mF cm^{-2} at 120 Hz. To overcome this bottleneck, we developed the GxCy hybrid gel system by incorporating 1D carboxylated multi-walled carbon nanotubes (MWCNTs). Leveraging the anchoring effect of MWCNTs, these 1D nanotubes are intercalated between the 2D graphene layers, which not only effectively prevents interlayer restacking but also constructs a more stable and open 3D interconnected fluid pathway. This synergistic effect significantly augments the ion-accessible surface area, leading to a substantial enhancement in specific capacitance while preserving the exceptional high-frequency response.

The schematic in Fig. 2a outlines the synthesis of nitrogen-doped reduced graphene oxide/carboxylated multi-walled carbon nanotube composite gel membranes, denoted as GxCy (where x and y represent the mass ratios of GO to carboxylated MWCNTs; the hydrothermally reduced pure GO and MWCNT gel membranes are denoted as rGG and rCNT, respectively). To achieve oriented self-assembly into the gel membranes, these GO and carboxylated MWCNT dispersions with different ratios underwent hydrothermal reduction in the presence of ammonia and hydrazine hydrate, followed by direct vacuum filtration.[23] During the hydrothermal process, the oxygen-containing functional groups of the GO nanosheets and MWCNT walls provided abundant reactive sites for subsequent chemical modification and structural anchoring between each other, facilitating a synchronous deoxygenation and nitrogen-doping process. The synergistic interaction between the liquid-phase precursors plays a key role in the construction of the 3D framework. Within this confined reaction space, the one-dimensional (1D) carbon nanotubes and two-dimensional (2D) graphene nanosheets undergo spontaneous self-assembly, a process driven by π–π stacking interactions and covalent cross-linking facilitated by the formation of amide linkages between nitrogen-containing species and carboxyl groups. The thickness of the resulting membranes was found to be highly sensitive to the mass ratio of the precursors. Under identical mass loading, the pure rGG^0 membrane exhibited a minimum thickness of 9 μm, while the incorporation of MWCNTs progressively increased the thickness to 11 μm for $G4C1^0$, 13 μm for $G2C1^0$, 19 μm for $G1C1^0$, and reaching 28 μm for the pure $rCNT^0$ origin gel membrane. This monotonic increase in thickness directly manifests the spacer effect introduced by the nanotubes, which prevents the dense restacking of graphene and expands the interlaminar volume. Subsequently, after undergoing the same sulfuric acid

exchange/vacuum drying treatment as rGG^0, the corresponding G4C1, G2C1, G1C1, and rCNT gel based EDLCs were obtained.

The morphological transformation from dense stacking to a 3D network was characterized by SEM (Fig. 2b and S4). Although the closely-packed sheet structure is conducive to the direct conduction of electrons within the plane, it is not favorable for the rapid transmission of ions because the electrolyte has difficulty accessing the internal pores, especially under the influence of high-frequency alternating current. The introduced MWCNTs in the G4C1 composite gel membrane slightly disrupt the ordered alignment of graphene, while forming stacked graphene domains alongside locally loosened CNT-rich regions. This suggests that nanotubes can weaken graphene restacking and create open areas, whereas the majority remain covered within the graphene layers, failing to establish an optimal open-pore network. In contrast, a breakthrough in structural evolution occurs at the G2C1 ratio. In this optimized configuration, MWCNTs are uniformly distributed between the rGO nanosheets, acting as structural pillars that open the interlaminar spaces. It leads to the formation of an interconnected 3D porous framework rich in mesopores, which is critical for minimizing ion-transport resistance by providing vertical channels for rapid ionic transportation. As the MWCNT content further increases in G1C1, the excessive nanotubes dismantle the graphene framework, resulting in a disordered and curled morphology where nanosheets are isolated by loosened nanotube clusters. The pure rCNT membrane displays a loosely entangled and highly porous network that lacks the continuous electronic pathways inherently provided by graphene nanosheets.

The structural variation of these gel membranes is further corroborated by X-ray diffraction (XRD) patterns (Fig. 2c), which probe the long-range ordering of the carbon stacking. The rGG membrane exhibits a distinct diffraction peak related to the (002) plane at $2\theta = 23.5°$, corresponding to an interlayer d-spacing of approximately 0.38 nm, which indicates a significant re-graphitization degree and ordered stacking during reduction. Similarly, the rCNT membrane shows a sharp peak at $2\theta = 26°$, consistent with the highly crystalline nature of the MWCNT walls. Crucially, the composite membranes, particularly G2C1, display an amorphous-like feature characterized by a very broad and low-intensity scattering signal between 22° and 29°. Compared with the rGG membrane, the disordered stacking of graphene layers in G2C1 reveals that the rGO is well separated from the MWCNTs. The incorporation of MWCNTs effectively disrupts the coherent stacking of rGO sheets, establishing a macroscopically continuous, porous architecture that simultaneously enhances ionic accessibility and preserves mechanical integrity. Complementary to the XRD findings, Raman spectroscopy was employed to evaluate the degree of structural disorder and defect density,[26] as shown in Fig. 2d. The intensity ratio of the D and G peaks (I_D/I_G) of the membranes follows a specific sequence: rGG (1.40) > G4C1 (1.35) > G2C1 (1.31) > G1C1 (1.22) > rCNT (1.07). The highest I_D/I_G ratio for pure rGG reflects the high concentration of structural defects and edges generated during the intensive hydrothermal reduction of GO. As lower-defect MWCNTs are incorporated, the average I_D/I_G ratio of the composite decreases, indicating that the successful intercalation of MWCNTs into GO layers forms an interface through hydrogen bonding and π–π stacking. For G2C1, the ratio of 1.31 suggests a balanced state where enough sp^2 domains are preserved to ensure rapid electronic conduction, while defective sites suggest that the anchored MWCNTs construct open channels that facilitate ion diffusion. This balance is critical for high frequency applications, where both electronic and ionic transport must be optimized simultaneously to minimize the time constant τ ($\tau = RC$) for the high-performance filtering capacitors.

The surface chemistry and elemental composition of the membranes, as determined by X-ray photoelectron spectroscopy (XPS), provide a deeper understanding of the chemical synergy within these membrane architectures. As shown in Fig. S5, the XPS survey spectra reveal distinct changes in the surface elemental composition with varying rGO/MWCNT ratios. The corresponding O/C ratios of rGG, G4C1, G2C1, G1C1, and rCNT are 0.191, 0.185, 0.234, 0.226, and 0.274, while the N/C ratios are 0.048, 0.042, 0.057, 0.042, and 0.044, respectively. These data indicate that rGG and G4C1 possess carbon-rich and oxygen-poor surfaces, suggesting that these gels are dominated by reduced conjugated carbon frameworks. rCNT shows the highest oxygen content, which is fully consistent with the surface chemistry expected for acid-treated carboxylated MWCNTs (Fig. S6). The elemental survey reveals that G2C1 possesses the highest nitrogen content (4.41%) and the highest N/C ratio (0.057) among all samples, exceeding even the pure rGG (3.91%) and rCNT (3.31%). The C 1s spectra (Fig. S7) provide deeper insight into the local carbon environments and clarify these surface compositions. The dominant C–C/C=C contribution (49.97%) manifests the strongest recovery of the sp^2-conjugated carbon framework among all samples, while the very small O=C–OH fraction (0.28%) suggests that most high-oxidation-state edge groups have been removed during the reduction process. By contrast, the content of O=C–OH in rCNT is around 4.11%, consistent with the oxygen-rich edge and defect chemistry of acid-treated nanotubes. Most importantly, G2C1 exhibits the highest O=C–OH contribution (5.45%) among all samples, indicating the greatest preservation of effective carboxyl-containing interfacial sites arising from the carboxylated nanotubes and the edge regions of reduced graphene sheets. At the same time, it also manifests the anchoring and coupling between the 2D graphene sheets and the 1D nanotube spacers. Notably, these oxygenated groups improve electrolyte wettability, which is critical for improving the ion accessibility.[27] In addition, the highest C–N content of G2C1 suggests the most sufficient interfacial nitrogen functionalization under the ammonia/hydrazine hydrothermal treatment. Therefore, the surface chemistry of G2C1 is not merely a partially reduced state, but rather an optimized interfacial state with enhanced chemical coupling and ion-accessible polarity.

As shown in Fig. 2e and S8, the N 1s spectra, deconvolution into pyrrolic-N (399.7 eV), amino-N (400.3 eV), and quaternary-N (401.4 eV), unveil the chemical nature of the nitrogen species.[28,29] The rCNT membrane is dominated by amino-N (49.3%), which originates from the surface amidation of the

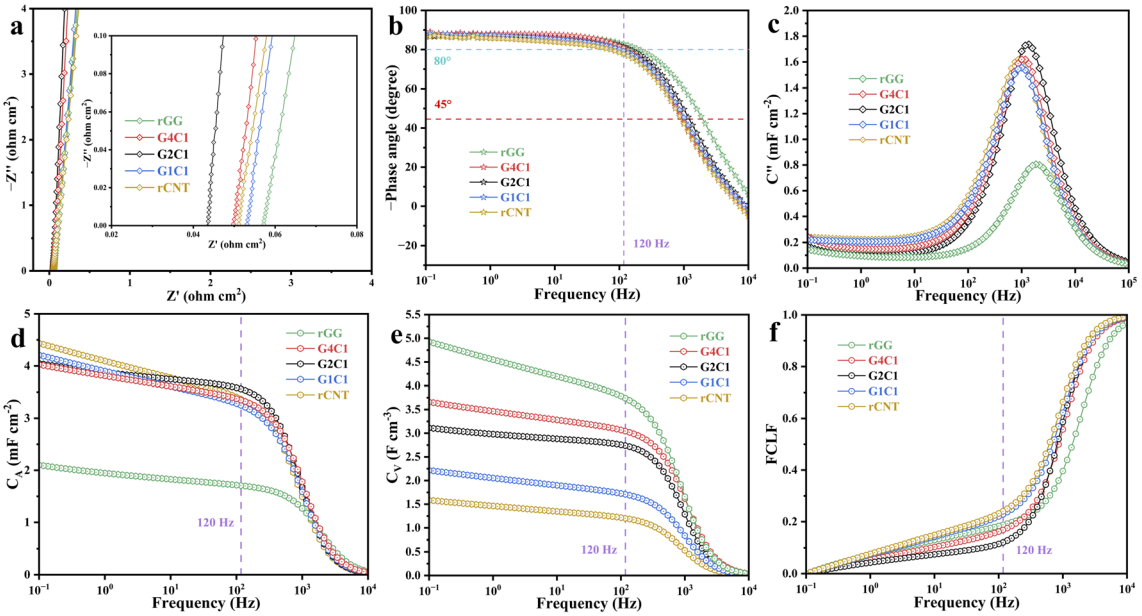

Fig. 3 Electrochemical frequency response and capacitive performance. (a) Nyquist plot (inset: an enlarged view of the high frequency region), (b) −phase angle *versus* frequency, (c) frequency-dependent imaginary capacitance (C'') curves, (d) areal capacitance (C_A), (e) volumetric capacitance (C_V) and (f) frequency-dependent capacitance loss factor (FCLF) of rGG, G4C1, G2C1, G1C1 and rCNT based symmetrical EDLCs, respectively (mass loading: 0.05 mg cm^{-2}).

O═C–OH groups. In contrast, the high proportion of amino-N (56.0%) in G2C1 further manifests the effectively anchoring of MWCNTs in rGO, which is in agreement with Raman results. These XPS findings provide a chemical explanation for the superior kinetic performance of G2C1; it combines the best features of both precursors, namely the high doping density of rGO and the structural stability of rCNT. The conductivity of the membranes was evaluated using the four-probe conductivity measurement method. In comparison, the GxCy gel electrodes still exhibited a high conductivity of >100 S m^{-1} (Fig. S9), which is sufficient to meet the good electronic response at 120 Hz. Interestingly, G2C1 does not possess the highest conductivity despite its optimized structure, which is ascribed to the most open and amorphous-like porous structure (as confirmed by XRD). A lower packing density results in lower electrical conductivity, which follows the inverse relationship between material density and apparent conductivity. The dense rGG and G4C1 membranes have higher volumetric carbon densities, which facilitate more direct contact between sp^2 domains in the interlayer spaces. However, as demonstrated by the subsequent electrochemical tests, this moderate conductivity is more than sufficient for high-frequency filtering, while the benefits of its 3D open structure for ion transport far outweigh the slight reduction in electronic conduction.

The electrochemical performance was comprehensively evaluated using Electrochemical Impedance Spectroscopy (EIS), which is the most direct method for evaluating filtering capability at 120 Hz, as shown in Fig. 3a. The Nyquist plots for all membranes exhibit near-vertical lines in the low-frequency region, signifying nearly ideal electric double-layer capacitive behavior. Notably, there are no discernible semicircles in the high-frequency region, indicating that the charge-transfer resistance is negligible for these carbon-based electrodes. The series resistance R_s, determined by the high-frequency intercept on the real axis, reveals a crucial trend: G2C1 possesses the lowest the series resistance R_s of 43.5 mΩ cm^2, which is significantly lower than that of rGG (57.2 mΩ cm^2), G4C1 (49.8 mΩ cm^2), G1C1 (52.9 mΩ cm^2), and rCNT (51.1 mΩ cm^2). In the electrolyte-filled state, the total resistance is dominated by the ionic transport within the pores. The open 3D framework of G2C1 provides a much less tortuous path for ion migration compared to dense rGG, effectively lowering the overall impedance of the system during actual operation. The frequency response was further analyzed using Bode plots (Fig. 3b). For 120 Hz filtering, the phase angle should ideally be as close to −90° as possible. All samples showed outstanding high-frequency stability, with phase angles at 120 Hz ranging from −77.73° (rCNT) to −82.9° (rGG), with G2C1 achieving a competitive −81.1°. To further decouple the capacitive and resistive contributions, the complex capacitance model was employed. The imaginary component $C''(f)$, which reflects energy dissipation due to irreversible processes, reaches its resonant maximum at the characteristic frequency f_0. As shown in Fig. 3c, the derived f_0 values follow the order: rGG (2030 Hz) > G2C1 (1359 Hz) > G4C1 (1142 Hz) > G1C1 (1000 Hz) > rCNT (882 Hz). The corresponding characteristic time constants τ_0, which represent the minimum time required to discharge the stored energy with an efficiency of over 50%, were calculated to be 0.493 ms (rGG), 0.736 ms (G2C1), 0.876 ms (G4C1), 1 ms (G1C1), and 1.13 ms (rCNT). Critically, all membranes achieved τ_0 values significantly below the 8.33 ms threshold required for 120 Hz AC line-filtering. However, a purely kinetic comparison is insufficient for practical device design. While the rGG membrane exhibits the fastest τ_0 (0.493 ms), its areal

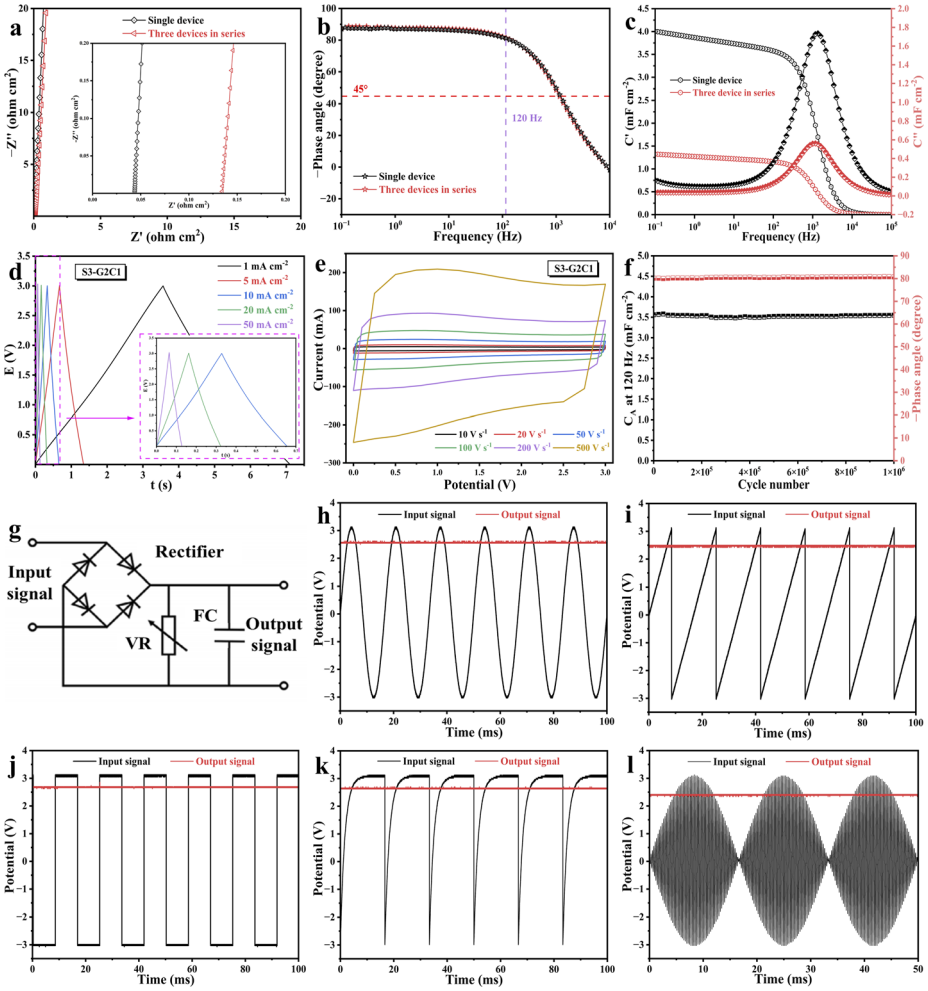

Fig. 4 Device scalability, long-term stability, and practical AC line-filtering applications. (a) Nyquist plots, (b) Bode plots, and (c) real and imaginary parts of capacitance *versus* frequency plots comparing a single G2C1 based EDLC with three EDLCs in series (S3-G2C1). (d) GCD curves at different current densities and (e) CV profiles up to 500 V s^{-1} of S3-G2C1. (f) Stability of C_A and −phase angle at 120 Hz with a long-term GCD test (50 mA cm^{-2}) of the single G2C1 based EDLC over 1 million cycles. (g) Schematic demonstration of the circuit used for smoothing AC signals (the resistance of the variable resistor used is 1 kΩ). (h–l) Filtering performance of the three G2C1 based EDLCs in series.

capacitance (C_A) is severely compromised by its inaccessible internal surface area, as shown in Fig. 3d. G2C1, on the other hand, delivers C_A of 3.56 mF cm^{-2}, which is a 108% increase over rGG (1.71 mF cm^{-2}). G2C1 achieves the optimal balance by maximizing the utilized surface area of the rGO sheets through the spacer effect of MWCNTs, providing the highest areal capacitance while maintaining an ultra-fast time constant of 0.736 ms. This ensures that the G2C1 based filtering capacitor can provide sufficient smoothing power while occupying a minimal footprint on a circuit board. All in all, G2C1 provides sub-millisecond kinetics while retaining a high charge-storage capacity, thus improving the kinetic-capacity trade-off that plagues traditional dense carbon electrodes. Furthermore, the dissipation factor (DF) of G2C1 has a very small value of about 0.1 at 120 Hz (Fig. S10), suggesting a slight loss characteristic of the devices.

Meanwhile, the volumetric capacitance (C_V) was also calculated (Fig. 3e). The C_V values follow the sequence: rGG (3.74 F cm^{-3}) > G4C1 (3.05 F cm^{-3}) > G2C1 (2.74 F cm^{-3}) > G1C1 (1.71 F cm^{-3}) > rCNT (1.20 F cm^{-3}). The higher C_V of rGG is attributed to its extreme thinness and density, but its low total areal capacitance limits its practical application in miniaturized filtering circuits. To more intuitively demonstrate the difficulty of forming double-layer capacitance at high frequencies in different electrode material structures, we subsequently used the proportion of capacitance reduction at high frequencies to compare the loss of capacitance caused by frequency changes (*i.e.*, the frequency capacitance loss factor, FCLF, Fig. 3f). As this factor approaches zero, capacitance retention increases, interfacial ionic resistance decreases, and interlayer ion transport connectivity is enhanced. These C_A and C_V values ($-\varphi > 80°$) exceed those of the majority of previously documented sandwich filtering capacitors (Fig. S11).

The optimal G2C1 was selected for comprehensive evaluation of tandem performance, rate capability, cycling stability, and AC line-filtering. To explore its potential for high-voltage

applications, three G2C1 based EDLCs were connected in series (denoted as S3). In the Nyquist plots (Fig. 4a), the S3 device maintains a near-vertical characteristic relative to the real axis, consistent with the single device (S1), with the intercept resistance increasing proportionally. Notably, as shown in Fig. 4b, the Bode plots of S1 and S3 exhibit highly overlapping phase angle profiles, both sustaining a significant phase angle of −81° at 120 Hz, indicating that the high-frequency response is preserved upon tandem integration. Within the complex capacitance model (Fig. 4c), the real part $C'(f)$ represents the accessible capacitance at a given frequency, while the imaginary part $C''(f)$ reflects energy dissipation due to irreversible diffusion and polarization processes. The G2C1 electrode enables the device to retain high capacitance values even beyond 120 Hz. Specifically, the capacitance of S1 is approximately three times that of S3, aligning perfectly with the theoretical laws of series-connected capacitors. Most significantly, both S1 and S3 reach their maximum $C''(f)$ values at the same peak frequency (f_0 = 1359 Hz), yielding an ultra-short characteristic time constant. This consistency further validates that high-performance, high-voltage filtering can be seamlessly achieved through the tandem integration of G2C1 based EDLCs.

Furthermore, the galvanostatic charge–discharge (GCD) curves of S3 exhibit an ideal linear profile with negligible *iR* drop even at a high current density of 50 mA cm^{-2} (Fig. 4d), signifying exceptional rapid charge–discharge capability. This low internal resistance matches the ultrafast ionic kinetics, a phenomenon corroborated by the minimal polarization observed in cyclic voltammetry (CV), as shown in Fig. 4e. The CV curves of S3 remain rectangular even at an extraordinary scan rate of 500 V s^{-1}, demonstrating superior electron transport dynamics and the mechanical integrity of the G2C1 network. Long-term reliability was also confirmed *via* over 1 000 000 continuous GCD cycles for S1 (Fig. 4f); no discernible degradation in capacitance or phase angle at 120 Hz was observed, highlighting the outstanding durability of the 1D/2D composite. This stability is directly attributed to the robust 3D interconnected framework, which prevents the structural collapse or ion-path blockage during rapid charge–discharge cycles. In a practical AC line-filtering simulation, the G2C1 based filtering capacitor was subjected to a 120 Hz AC ripple voltage (Fig. 4g). The resulting output voltage waveform demonstrated the device's superior smoothing ability, converting the erratic AC signal into a stable DC output with a negligible ripple factor. The R_s of the assembled G2C1 supercapacitor remained within the milliohm range, ensuring that internal power loss and heat generation were kept at a minimum. Crucially, the experimental results further confirm that S3 exhibits excellent AC line-filtering performance (Fig. 4h–l). In the filtering demonstration circuit, S3 is connected in parallel with the load resistor (1 kΩ) and located at the end of the full-bridge rectifier circuit. This system successfully converts the pulsating DC signal generated by rectification of the AC input after the full-bridge rectifier into a stable DC output. Under the above test conditions, the output ripple voltage is only 38 mV, fully demonstrating the outstanding ability of this material to suppress high-frequency fluctuations and smooth the current output.

Conclusions

In summary, we have successfully developed a gel strategy to construct a 3D rGO/MWCNT framework featuring ionic fluid channels, specifically tailored for AC line-filtering. By integrating 1D MWCNTs into the 2D rGO matrix, the inherent restacking of graphene sheets was effectively inhibited, resulting in an interconnected and stable 3D open network. The highly interconnected fluid channels within the gel provide a continuous liquid-phase path with low-resistance for fast ion transport into deep active sites in a shorter time, achieving both high frequency and high capacity simultaneously. This structural modification ensures a high-density electron transport pathway and ultra-fast ionic accessibility, demonstrating that the electrochemical performance is governed by a synergistic balance among conductive continuity, interfacial wettability, and open ion-transport channels. The optimized electrode manifests an exceptionally low series resistance of 43.5 mΩ cm^2 and a remarkable areal capacitance of 3.56 mF cm^{-2} at 120 Hz, accompanied by a near-ideal phase angle of −81.1°. This work effectively improves the trade-off between capacity and response speed, providing a robust design principle for engineering advanced carbon-based electrochemical capacitors for next-generation miniaturized power electronics.

Author contributions

J. Z. and Z. W. conceived, designed, and wrote the manuscript. X. Y. discussed the results and guided the project. All authors commented on the manuscript and approved the submission.

Conflicts of interest

There are no conflicts to declare.

Data availability

The data supporting the findings of this study are available within the paper and its supplementary information (SI). Supplementary information: experimental methods for materials synthesis; schematics of the Gel-EDLC preparation process; materials characterization; electrochemical measurements & calculations; additional characterization results of rGG, G4C1, G2C1, G1C1, and rCNT gel membranes, respectively. See DOI: https://doi.org/10.1039/d6sc02703b.

Acknowledgements

This work was supported by the National Key Research and Development Program of China (2021YFA1101300), the National Natural Science Foundation of China (No. 52302241), and the China Postdoctoral Science Foundation (No. 2023M730940).

Notes and references

1 J. R. Miller, R. A. Outlaw and B. C. Holloway, *Science*, 2010, **329**, 1637–1639.
2 J. Park and W. Kim, *Adv. Energy Mater.*, 2021, **11**, 2003306.
3 P. Simon and Y. Gogotsi, *Nat. Mater.*, 2008, **7**, 845–854.
4 D. Pech, M. Brunet, H. Durou, P. Huang, V. Mochalin, Y. Gogotsi, P. L. Taberna and P. Simon, *Nat. Nanotechnol.*, 2010, **5**, 651–654.
5 H. Tang, Y. Tian, Z. Wu, Y. Zeng, Y. Wang, Y. Hou, Z. Ye and J. Lu, *Energy Environ. Mater.*, 2022, **5**, 1060–1083.
6 F. Han, O. Qian, G. Meng, D. Lin, G. Chen, S. Zhang, Q. Pan, X. Zhang, X. Zhu and B. Wei, *Science*, 2022, **377**, 1004–1007.
7 S. Xu, Y. Wen, Z. Chen, N. Ji, Z. Zou, M. Wu, L. Qu and J. Zhang, *Angew Chem. Int. Ed. Engl.*, 2021, **60**, 24505–24509.
8 W. Li, S. Azam, G. Dai and Z. Fan, *Energy Storage Mater.*, 2020, **32**, 30–36.
9 N. Islam, S. Li, G. Ren, Y. Zu, J. Warzywoda, S. Wang and Z. Fan, *Nano Energy*, 2017, **40**, 107–114.
10 M. Wu, F. Chi, H. Geng, H. Ma, M. Zhang, T. Gao, C. Li and L. Qu, *Nat. Commun.*, 2019, **10**, 2855.
11 Z. Li, X. Wang, L. Zhao, F. Chi, C. Gao, Y. Wang, M. Yan, Q. Zhou, M. Zhao, X. Wang, J. Wang, M. Yuan, M. Wu, L. Wang, Y. Zhao and L. Qu, *Nat. Commun.*, 2022, **13**, 6359.
12 Y. Rangom, X. S. Tang and L. F. Nazar, *ACS Nano*, 2015, **9**, 7248–7255.
13 Y. Cao, Z. Xiong, F. Xia, G. V. Franks, L. Zu, X. Wang, Y. Hora, S. Mudie, Z. He, L. Qu, Y. Xing and D. Li, *Adv. Funct. Mater.*, 2022, **32**, 2201535.
14 L. Li, S. Yang, K. Xia, M. Chen, Y. Zhuang, W. Zhu, Q. Huang, Y. Wang, X. Fan, W. Zhao, Z. Lu, Y. Wen, M. Wu and Z. Zou, *Adv. Funct. Mater.*, 2025, **35**, e10499.
15 M. Zhao, Y. Qin, X. Wang, L. Wang, Q. Jin, M. Song, X. Wang and L. Qu, *Adv. Funct. Mater.*, 2023, **34**, 2313495.
16 G. Chen, F. Han, H. Ma, P. Li, Z. Zhou, P. Wang, X. Li, G. Meng and B. Wei, *Nano-Micro Lett.*, 2024, **16**, 235.
17 M. Wu, K. Sun, J. He, Q. Huang, W. Zhan, Z. Lu, M. C. Xia, Y. Zhang, X. Lyu, H. Geng, Z. Z. Luo and Z. Zou, *Adv. Funct. Mater.*, 2023, **33**, 2305039.
18 Y. Wang, Y. Zhang, G. Wang, X. Shi, Y. Qiao, J. Liu, H. Liu, A. Ganesh and L. Li, *Adv. Funct. Mater.*, 2020, **30**, 1907284.
19 X. Liu, Q. Wang, J. Cui and Y. Yan, *Carbon*, 2025, 233.
20 L. Qiu, X. Yang, X. Gou, W. Yang, Z. F. Ma, G. G. Wallace and D. Li, *Chemistry*, 2010, **16**, 10653–10658.
21 J. M. Choi, J. Han, J. Yoon, S. Kim, I. Jeon and S. Maruyama, *Adv. Funct. Mater.*, 2022, **32**, 2204594.
22 J. Zhu, J. Hu, Z. Wang, Z. Lu, S. Das and P. Cool, *Chem. Sci.*, 2025, **16**, 2850–2860.
23 X. Yang, C. Cheng, Y. Wang, L. Qiu and D. Li, *Science*, 2013, **341**, 534–537.
24 X. Yang, L. Qiu, C. Cheng, Y. Wu, Z. F. Ma and D. Li, *Angew Chem. Int. Ed. Engl.*, 2011, **50**, 7325–7328.
25 X. Yang, J. Zhu, L. Qiu and D. Li, *Adv. Mater.*, 2011, **23**, 2833–2838.
26 J. Chen, Y. Zhang, M. Zhang, B. Yao, Y. Li, L. Huang, C. Li and G. Shi, *Chem. Sci.*, 2016, **7**, 1874–1881.
27 X. Chang, C. W. Lin, A. Huang, M. F. El-Kady and R. B. Kaner, *Nano Lett.*, 2023, **23**, 3317–3325.
28 J. Guo, X. Xu, J. P. Hill, L. Wang, J. Dang, Y. Kang, Y. Li, W. Guan and Y. Yamauchi, *Chem. Sci.*, 2021, **12**, 10334–10340.
29 Y. Lu, X. Li and R. G. Compton, *Chem. Sci.*, 2022, **13**, 1355–1366.